Tunable narrow-photon-energy X-ray generator utilizing a tungsten-target tube

Eiichi Sato[a,*], Hiroshi Sugiyama[b], Masami Ando[b], Etsuro Tanaka[c], Hidezo Mori[d], Toshiaki Kawai[e], Takashi Inoue[f], Akira Ogawa[f], Kazuyoshi Takayama[g], Jun Onagawa[h], Hideaki Ido[h]

[a]Department of Physics, Iwate Medical University, 3-16-1 Honchodori, Morioka 020-0015, Japan
[b]Photon Factory, Institute of Materials Structure Science, High Energy Accelerator Research Organization, 1-1 Oho, Tsukuba 305-0801, Japan
[c]Department of Nutritional Science, Faculty of Applied Bio-science, Tokyo University of Agriculture, 1-1-1 Sakuragaoka, Setagaya-ku 156-8502, Japan
[d]Department of Cardiac Physiology, National Cardiovascular Center Research Institute, 5-7-1 Fujishirodai, Suita, Osaka 565-8565 Japan
[e]Electron Tube Division #2, Hamamatsu Photonics K.K., 314-5 Shimokanzo, Iwata 438-0193, Japan
[f]Department of Neurosurgery, School of Medicine, Iwate Medical University, 19-1 Uchimaru, Morioka 020-8505, Japan
[g]Shock Wave Research Center, Institute of Fluid Science, Tohoku University, 2-1-1 Katahira, Sendai 980-8577, Japan
[h]Department of Applied Physics and Informatics, Faculty of Engineering, Tohoku Gakuin University, 1-13-1 Chuo, Tagajo 985-8537, Japan

Abstract

A preliminary experiment for producing narrow-photon-energy cone-beam X-rays using a silicon single crystal is described. In order to produce low-photon-energy X-rays, a 100-μm-focus X-ray generator in conjunction with a (1 1 1) plane silicon crystal is employed. The X-ray generator consists of a main controller and a unit with a high-voltage circuit and a microfocus X-ray tube. The maximum tube voltage and current were 35 kV and 0.50 mA, respectively, and the X-ray intensity of the microfocus generator was 48.3 μGy/s at 1.0 m from the source with a tube voltage of 30 kV and a current of 0.50 mA. The effective photon energy is determined by Bragg's angle, and the photon-energy width is regulated by the angle delta. Using this generator in conjunction with a computed radiography system, quasi-monochromatic radiography was performed using a cone beam with an effective energy of approximately 17 keV.
© 2006 Elsevier Ltd. All rights reserved.

1. Introduction

*Corresponding author.
E-mail address: dresato@iwate-med.ac.jp (E. Sato).

Since the birth of the synchrotron, monochromatic parallel X-ray beams have been applied to X-ray phase-contrast radiography (Davis et al., 1995; Momose et al.,

1996; Ando et al., 2002) and enhanced K-edge angiography (Thompson et al., 1992; Mori et al., 1996; Hyodo et al., 1998). The phase imaging is primarily based on the X-ray refraction, and the angiography is performed using X-rays with a photon energy of just beyond the K-absorption edge of iodine.

In order to perform high-speed medical radiography, although several different flash X-ray generators utilizing cold-cathode tubes have been developed (Sato et al., 1990, 1994a, b; Shikoda et al., 1994; Takahashi et al., 1994), quasi-monochromatic flash X-ray generators (Sato et al., 2003a, b, 2004a, b, 2005a–c) are useful to produce clean K-series characteristic X-rays without using a filter. Therefore, we have performed a demonstration of cone-beam K-edge angiography utilizing a cerium plasma generator, since K-series characteristic X-rays from the cerium target are absorbed effectively by iodine. In view of this situation, we have developed a steady state X-ray generator utilizing a cerium-target tube (Sato et al., 2004c), and have demonstrated enhanced K-edge angiography utilizing cerium $K\alpha$ lines.

Without using synchrotrons, X-ray phase-contrast radiography for edge enhancement has been performed using a microfocus X-ray tube (Wilkins et al., 1996), and the digital imaging achieved with a 100-μm-focus molybdenum tube has been applied effectively to perform mammography (Ishisaka et al., 2000).

In this paper, we present a tunable narrow-photon-energy X-ray generator utilizing a single silicon crystal, and examine its suitability for energy-selective cone-beam radiography.

2. Experimental setup

Fig. 1 shows the block diagram of the X-ray generator, which consists of a main controller and an X-ray tube unit with a Cockcroft–Walton circuit and a 100-μm-focus X-ray tube. The tube voltage, the current, and the exposure time can be controlled by the controller. The main circuit for producing X-rays is illustrated in Fig. 2, and employed the Cockcroft–Walton circuit in order to decrease the dimensions of the tube unit. In the X-ray tube, positive and negative high voltages are applied to the anode and cathode electrodes, respectively. The filament heating current is supplied by an AC power supply in the controller in conjunction with an insulation transformer. The maximum tube voltage and current of the generator are 105 kV and 0.50 mA, respectively. In this experiment, the tube voltage applied was from 18 to 34 kV, and the tube current was 0.50 mA (maximum current) by the filament temperature. The exposure time is controlled in order to obtain optimum X-ray intensity.

The narrow-photon-energy X-ray generator utilizing a single silicon crystal of (1 1 1) plane is shown in Fig. 3. The effective photon energy is determined by Bragg's angle, and the photon-energy width is regulated by the
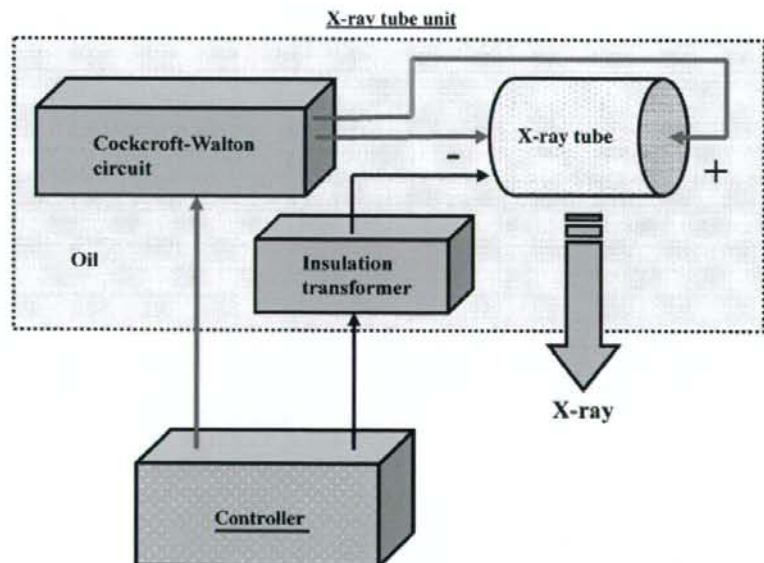

Fig. 1. Block diagram of a compact 100-μm focus X-ray generator with a tungsten-target radiation tube.
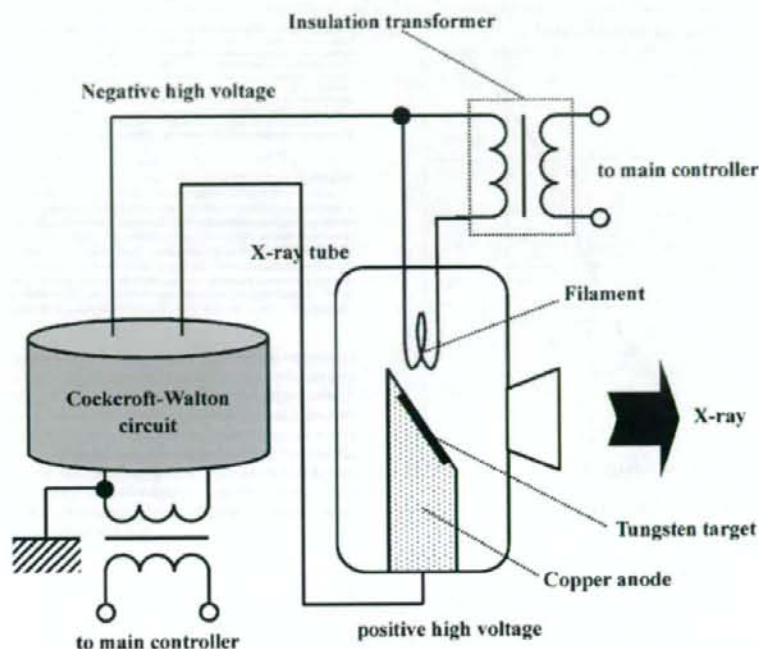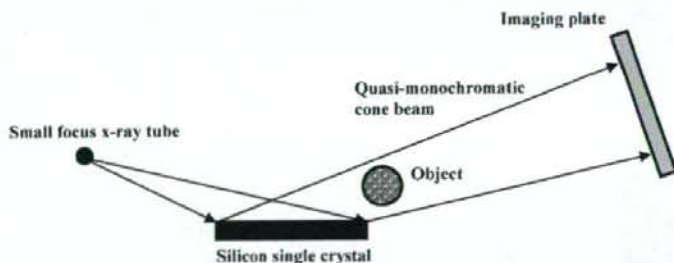
Fig. 2. Main circuit of the X-ray generator.

Fig. 3. Experimental setup of the narrow-photon-energy X-ray generator utilizing a single silicon crystal.

angle delta. Using this generator in conjunction with a computed radiography (CR) system (Sato et al., 2000), quasi-monochromatic radiography was performed using a cone beam with an effective energy of approximately 17 keV.

3. Results

3.1. X-ray intensity

X-ray intensity was measured by a Victoreen 660 ionization chamber at 1.0 m from the X-ray source

(Fig. 4). At a constant tube current of 0.50 mA, the X-ray intensity increased when the tube voltage was increased. In this measurement, the intensity with a tube voltage of 30 kV was 48.3 μGy/s at 1.0 m from the source.

3.2. Radiography

The radiography was performed by the CR system (Konica Minolta Regius 150) with a sampling pitch of 87.5 μm, and the conditions for radiography were as in Fig. 3. Fig. 5 shows the irradiation field diffracted by the crystal with photon energies of approximately 17 keV.
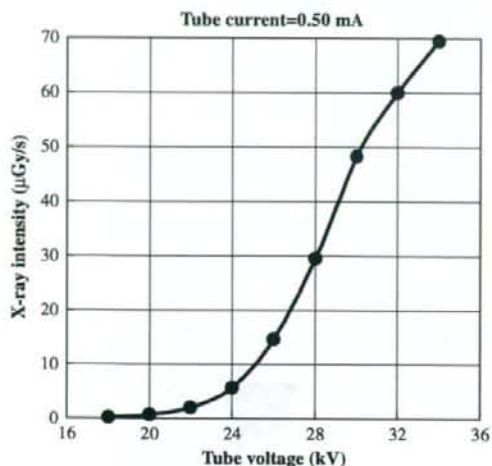
Fig. 4. X-ray intensity (µGy/s) as a function of tube voltage (kV) with a tube current of 0.50 mA.

Fig. 6. Radiogram of a lead test chart for measuring the spatial resolution.

Because the width of the irradiation field was narrow due to the angle, the distance between the crystal and the imaging plate should be increased. Fig. 6 shows a radiogram of a test chart for determining the spatial resolution. In this radiography, 100-µm-wide lead lines (5 line pair) were observed. Subsequently, fine bone structures were visible in radiograms of a vertebra (Fig. 7), and fine blood vessels were observed in an angiogram of a rabbit heart (Fig. 8).

4. Conclusion and outlook

In summary, we employed a 100-µm-fosus X-ray generator with a tungsten-target tube and succeeded in producing narrow-photon-energy bremsstrahlung X-rays, which are refracted by a silicon single crystal of (1 1 1) plane. The photon energy width is primarily determined by the distance between the X-ray source and the crystal plate, and the irradiation field increases with increases in the distance between the crystal and the imaging plate. Because we employed the microfocus tube, phase-contrast effect was added in the radiography.

The microfocus generator produced maximum X-ray intensity was approximately 50 µGy/s at 1.0 m from the source, but the intensity was decreased substantially after the diffraction. Therefore, a high-current tungsten tube with a large focus should be employed in cases where the phase-contrast radiography is not employed.
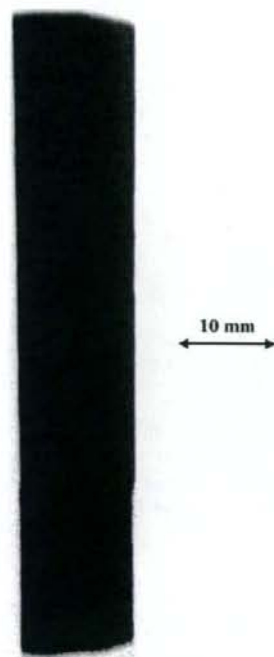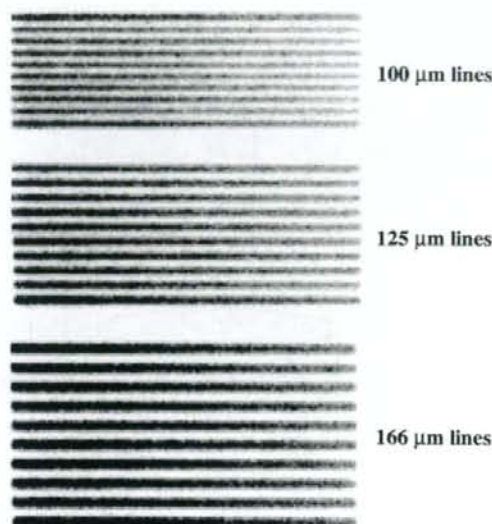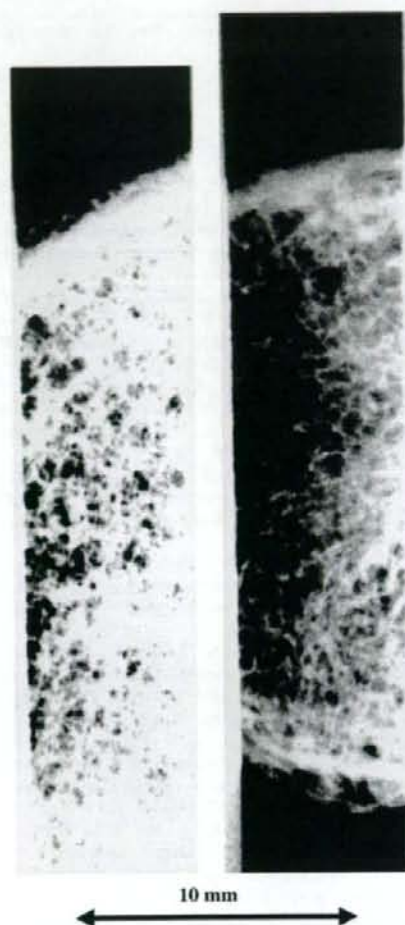

Fig. 5. Irradiation field with photon energies of approximately 17 keV measured using the CR system with a tube voltage of 30 kV.

Fig. 7. Radiograms of a vertebra.

Fig. 8. Angiogram of a rabbit heart.

narrow-photon-energy cone-beam radiography using a microfocus X-ray tube could be useful for phase-contrast radiography as an alternative to radiography using synchrotrons.

The magnification method is needed in phase-contrast radiography, and the method increases the spatial resolution of the digital radiography. Next, in conventional cohesion radiography, the spatial resolution is primarily determined by the sampling pitch of the CR system of $87.5\,\mu m$. Therefore, to improve the spatial resolution in cohesion radiography, the resolution of the CR system should be improved to approximately $50\,\mu m$ (Konica Minolta Regius 190). In addition, the spatial resolution can be improved easily to approximately $50\,\mu m$ or less in cases where an X-ray film is employed.

In this experiment, although we employed the (1 1 1) plane to perform soft radiography, other planes should be employed to perform high-photon-energy radiography. In conjunction with an analyzer crystal, this

References

Ando, M., Maksimenko, M., Sugiyama, H., Pattanasiriwisawa, W., Hyodo, K., Uyama, C., 2002. A simple X-ray dark- and bright- field imaging using achromatic Laue optics. Jpn. J. Appl. Phys. 41, L1016–L1018.

Davis, T.J., Gao, D., Gureyev, T.E., Stevenson, A.W., Wilkins, S.W., 1995. Phase-contrast imagimg of weakly absorbing materials using hard X-rays. Nature 373, 595–597.

Hyodo, K., Ando, M., Oku, Y., Yamamoto, S., Takeda, T., Itai, Y., Ohtsuka, S., Sugishita, Y., Tada, J., 1998. Development of a two-dimensional imaging system for clinical applications of intravenous coronary angiography using intense synchrotron radiation produced by a multi-pole wiggler. J. Synchrotron Rad. 5, 1123–1126.

Ishisaka, A., Ohara, H., Honda, C., 2000. A new method of analyzing edge effect in phase contrast imaging with incoherent X-rays. Opt. Rev. 7, 566–572.

Momose, A., Takeda, T., Itai, Y., Hirano, K., 1996. Phase-contrast X-ray computed tomography for observing biological soft tissues. Nature Med 2, 473–475.

Mori, H., Hyodo, K., Tanaka, E., Mohammed, M.U., Yamakawa, A., Shinozaki, Y., Nakazawa, H., Tanaka, Y., Sekka, T., Iwata, Y., Honda, S., Umetani, K., Ueki, H., Yokoyama, T., Tanioka, K., Kubota, M., Hosaka, H., Ishizawa, N., Ando, M., 1996. Small-vessel radiography in situ with monochromatic synchrotoron radiation. Radiology 201, 173–177.

Sato, E., Kimura, S., Kawasaki, S., Isobe, H., Takahashi, K., Tamakawa, Y., Yanagisawa, T., 1990. Repetitive flash X-ray generator utilizing a simple diode with a new type of energy-selective function. 2343–2348. Rev. Sci. Instrum. 61, 2343–2348.

Sato, E., Takahashi, K., Sagae, M., Kimura, S., Oizumi, T., Hayasi, Y., Tamakawa, Y., Yanagisawa, T., 1994a. Sub-kilohertz flash X-ray generator utilizing a glass-enclosed cold-cathode triode. Med. Biol. Eng. Comput. 32, 289–294.

Sato, E., Sagae, M., Takahashi, K., Shikoda, A., Oizumi, T., Hayasi, Y., Tamakawa, Y., Yanagisawa, T., 1994b. 10 kHz microsecond pulsed X-ray generator utilizing a hot-cathode triode with variable durations for biomedical radiography. Med. Biol. Eng. Comput. 32, 295–301.

Sato, E., Sato, K., Tamakawa, Y., 2000. Film-less computed radiography system for high-speed imaging. Ann. Rep. Iwate Med. Univ. Sch. Lib. Arts Sci. vol. 35, pp. 13-23.

Sato, E., Hayasi, Y., Germer, R., Tanaka, E., Mori, H., Kawai, T., Obara, H., Ichimaru, T., Takayama, K., Ido, H., 2003a. Irradiation of intense characteristic X-rays from weakly ionized linear molybdenum plasma. Jpn. J. Med. Phys. 23, 123–131.

Sato, E., Hayasi, Y., Germer, R., Tanaka, E., Mori, H., Kawai, T., Ichimaru, T., Takayama, K., Ido, H., 2003b. Quasi-monochromatic flash X-ray generator utilizing weakly

ionized linear copper plasma. Rev. Sci. Instrum. 74, 5236–5240.

Sato, E., Sagae, M., Tanaka, E., Hayasi, Y., Germer, R., Mori, H., Kawai, T., Ichimaru, T., Sato, S., Takayama, Y., Ido, H., 2004a. Quasi-monochromatic flash X-ray generator utilizing a disk-cathode molybdenum tube. Jpn. J. Appl. Phys. 43, 7324–7328.

Sato, E., Hayasi, Y., Germer, R., Tanaka, E., Mori, H., Kawai, T., Ichimaru, T., Sato, S., Takayama, K., Ido, H., 2004b. Sharp characteristic X-ray irradiation from weakly ionized linear plasma. J. Electron Spectrosc. Related Phenom. 137-140, 713–720.

Sato, E., Tanaka, E., Mori, H., Kawai, T., Ichimaru, T., Sato, S., Takayama, K., Ido, H., 2004c. Demonstration of enhanced K-edge angiography using a cerium target X-ray generator. Med. Phys. 31, 3017–3021.

Sato, E., Tanaka, E., Mori, H., Kawai, T., Ichimaru, T., Sato, S., Takayama, Y., Ido, H., 2005a. Compact monochromatic flash X-ray generator utilizing a disk-cathode molybdenum tube. Med. Phys. 32, 49–54.

Sato, E., Tanaka, E., Mori, H., Kawai, T., Sato, S., Takayama, Y., 2005b. High-speed enhanced K-edge angiography utilizing cerium plasma X-ray generator. Opt. Eng. 44, 049001–049016.

Sato, E., Tanaka, E., Mori, H., Kawai, T., Sato, S., Takayama, Y., 2005c. Clean monochromatic X-ray irradiation from weakly ionized linear copper plasma. Opt. Eng. 44, 049002–049016.

Shikoda, A., Sato, E., Sagae, M., Oizumi, T., Tamakawa, Y., Yanagisawa, T., 1994. Repetitive flash X-ray generator having a high-durability diode driven by a two-cable-type line pulser. Rev. Sci. Instrum. 65, 850–856.

Takahashi, K., Sato, E., Sagae, M., Oizumi, T., Tamakawa, Y., Yanagisawa, T., 1994. Fundamental study on a long-duration flash X-ray generator with a surface-discharge triode. Jpn. J. Appl. Phys. 33, 4146–4151.

Thompson, A.C., Zeman, H.D., Brown, G.S., Morrison, J., Reiser, P., Padmanabahn, V., Ong, L., Green, S., Giacomini, J., Gordon, H., Rubenstein, E., 1992. First operation of the medical research facility at the NSLS for coronary angiography. Rev. Sci. Instrum. 63, 625–628.

Wilkins, S.W., Gureyev, Gao, T.E., Pogany, D.A., Stevenson, A.W., 1996. Phase-contrast imaging using polychromatic hard X-rays. Nature 384, 335–338.

Original article

Long-term monitoring of pulmonary arterial pressure in conscious, unrestrained mice

Daryl O. Schwenke [a,*], James T. Pearson [b], Hidezo Mori [a], Mikiyasu Shirai [c]

[a] *Department of Cardiac Physiology, National Cardiovascular Center Research Institute, 5-7-1 Fujishirodai, Suita, Osaka 565-8565, Japan*
[b] *Department of Physiology, Monash University, Melbourne, Australia*
[c] *Faculty of Health Sciences, Hiroshima International University, Hiroshima, Japan*

Abstract

Introduction: The ability to genetically engineer specific gene 'knock-out' mice has provided a powerful tool for investigating the various mechanisms that contribute to the pathogenesis of pulmonary arterial hypertension (PAH). Yet, so far there have been no reports describing the measurement of pulmonary arterial pressure (PAP) in the conscious wild type mouse—an essential requirement for monitoring dynamic changes associated with the pathogenesis of PAH. Therefore, in this study we describe a new technique for long-term measurement of PAP in conscious unrestrained mice using telemetry. **Methods:** In five male C57BL/6 mice (B.W. 25–30 g), the sensing catheter of a telemetric transmitter was inserted into the right ventricle and advanced into the pulmonary artery. The transmitter body was positioned either within the abdominal cavity or subcutaneously on the back. During recovery from surgery, mean PAP was recorded daily for 1 week. Subsequently, the PAP responses to acute hypoxia (8% O_2 for 10 min) and L-NAME (50 mg/kg, s.c.) were tested in three mice. **Results:** By 1-week post surgery, all mice had fully recovered from surgery and baseline MPAP was stable at 14.9 ± 0.7 mm Hg. Additionally, the pulmonary vascular stimulants acute hypoxia and L-NAME provoked a 63% and 86% increase MPAP, respectively. **Discussion:** In summary, this study has demonstrated the ability to accurately measure PAP by telemetry in conscious, unrestrained mice. One important application of this technique for future studies is the possibility to assess the relative contribution of specific genes (using 'knock-out' mice) during the chronic development of pulmonary pathological conditions.
© 2005 Elsevier Inc. All rights reserved.

Keywords: Acute hypoxia; Conscious mouse; L-NAME; Pulmonary arterial pressure

1. Introduction

The mechanisms responsible for the pathogenesis of pulmonary arterial hypertension (PAH) are still not fully understood. In order to investigate potential underlying mechanisms, numerous studies have used pharmacological intervention to selectively block receptor or cellular pathways (e.g. nitric oxide—NO) involved in the modulation of pulmonary vascular tone (Ao, Huang, Zhu, Xiong, & Wang, 2004; Hampl, Archer, Nelson, & Weir, 1993; Hampl, Tristani-Firouzi, Nelson, & Archer, 1996; Huang, Wu, Kang, & Lin, 2002; Weissmann et al., 2001).

In the last decade, the ability to produce targeted gene mutations in the mouse has provided a powerful tool for studying physiological and pathophysiological pathways without pharmacological intervention. Accordingly, various strains of 'knock-out' mice that lack, for example, an isoform of nitric oxide synthase (NOS), have been used for investigating the pathogenesis of PAH (Fagan, Fouty et al., 1990; Fagan, Tyler et al., 1990; Li, Laubach, & Johns, 2001; Quinlan et al., 2000). Thus far, most data have been obtained from in vitro studies, and while such data have aided our understanding of PAH, in vivo studies, in particular using conscious mice, are also essential for investigating the chronic physiological changes within the whole organism, especially during the various developmental stages of PAH.

One of the limiting factors for investigating cardiovascular dynamics in a conscious mouse is its small size. Nevertheless,

* Corresponding author. Tel.: +81 6 6833 5012x2381; fax: +81 6 6835 5416.
  E-mail address: schwenke@ri.ncvc.go.jp (D.O. Schwenke).

numerous studies have reported the successful use of telemetry for the long-term measurement of systemic arterial pressure in the conscious mouse (Butz & Davisson, 2001; Mills et al., 2000; Tank et al., 2004; Van Vliet, Chafe, & Montani, 2003; Xue, Pamidimukkala, & Hay, 2005).

To date, there is a paucity of literature describing the in vivo measurement of pulmonary arterial pressure (PAP) in the mouse. Several studies have used an anaesthetized preparation, with either a closed- or open-chest model in order to measure PAP in vivo (Champion, Villnave, Tower, Kadowitz, & Hyman, 2000; Steudel et al., 1997; Zhao, Long, Morrell, & Wilkins, 1999). However, the ability to measure pulmonary arterial dynamics in conscious, freely moving mice to, firstly, avoid the depressive effects inherent with the use of anaesthesia and, secondly, to monitor the transient changes in PAP during the development of pathological conditions remains an essential objective in this field of research.

In this study we describe, for the first time, the technique of measuring PAP in the conscious mouse using telemetry. Indwelling catheters have been used for monitoring some cardiovascular variables (e.g. right ventricular pressure) in the conscious mouse (Campen, Shimoda, & O'Donnell, 2005). However, care is required when interpreting data collected using indwelling catheters due to the stress and anxiety associated with the restraint required (Hess, Clozel, & Clozel, 1996). In comparison, the use of telemetry provides more efficient and reliable measurements from freely moving mice (Butz & Davisson, 2001; Mills et al., 2000). Therefore, the protocol we describe in this study uses a commercially available telemetry and data acquisition system to record the systolic, diastolic and mean pulmonary arterial pressure as well as heart rate (HR) of conscious mice.

2. Methods

2.1. Animals

All experiments were approved by the local Animal Ethics Committee and conducted in accordance with the guidelines of the Physiological Society of Japan. Data were collected from five male C57BL/6 mice (~16 weeks old; B.W. 25–30 g). All mice were on a 12-h light/dark cycle at 25 ± 1 °C and were provided with food and water ad libitum.

2.2. Anaesthesia and surgical preparation

All surgical procedures were performed using standard aseptic techniques. Mice were anaesthetized with pentobarbital sodium (60 mg/kg, i.p.) such that the limb withdrawal reflex could not be elicited for the entire surgical period (~90 min). During surgery, body temperature was maintained at 38 °C using a rectal thermistor coupled with a thermostatically controlled heating pad (model BWT-100, BRC Ltd, Tokyo, Japan).

Following anaesthesia induction, the trachea was intubated using a 22-gauge BD Angiocath catheter (Becton Dickinson Inc., Utah, USA) and the lungs were ventilated using a mouse ventilator (Minivent Type 845, Hugo Sachs Elektronik

Harvard Apparatus, Germany). The inspirate was enriched with O_2 (~50% O_2) and the ventilator settings were set for a tidal volume of 225 µl and a respiratory frequency of 180 breaths/min.

All surgical areas were shaved and disinfected. The mouse was placed in a supine position and a 2-cm horizontal skin incision was made from the sternum parallel to the 3rd rib on the right side. The right pectoralis major and minor muscles were exposed and retracted. Subsequently, a right thoracotomy was made between the 3rd and 4th rib by blunt dissection.

2.2.1. Positioning of transmitter body

In two mice that had a B.W. of 30 g the body of the telemetric transmitter was placed in the abdominal cavity. The abdomen was opened with a midline abdominal laparotomy and the body of the transmitter was placed into the abdominal cavity. A blunted 21-gauge needle was used as a trocar to pass the transmitter catheter, subcutaneously, from the abdominal incision to the thorax cavity. The abdominal laparotomy was sutured closed.

In the remaining mice (B.W. <30 g), it was considered that the transmitter body would be too big to comfortably fit in the abdominal cavity and, thus, it was positioned subcutaneously on the top of the back. Mice were rolled onto their left side and a dorsal midline incision was made along the back, and the transmitter was placed within the cavity. The transmitter was loosely sutured to the lateral muscles along the back to prevent movement of the transmitter. The transmitter catheter was then passed, subcutaneously, from the back skin incision to the thorax cavity.

With the mouse in a supine position, the 3rd and 4th rib were retracted to expose the right ventricle. A 25-gauge needle was used to gently pierce the conus of the ventricle wall after which the tip of the transmitter catheter (~0.4 mm, thin-walled thermoplastic membrane) was inserted into the right ventricle. Prior to insertion of the catheter, the transmitter was activated (by magnet) and recording of the transmitted signal initiated. Once the catheter was in the ventricle it was slowly advanced anteriorly towards the pulmonary artery until confirmation of its position within the pulmonary artery was evident by monitoring the change in pressure signal. A purse-string tie using 7.0 Prolene suture was used to fix the catheter to the surface of the ventricle wall. The catheter was also externally secured to the 4th and 5th rib for added support. Finally, the thoracotomy was closed with 6.0 silk-thread and all skin incisions were closed with 6.0 Prolene nylon suture.

Immediately following surgery, each mouse received 50 mg/kg (i.m.) of Viccillin® antibiotic (Meiji Seika Kaisha, Ltd, Tokyo Japan) and remained on the heating blanket during recovery from anaesthesia. Mice were gradually weaned off the ventilator when signs of consciousness were evident. However, the weaning time was extended by several hours if any form of sedation/analgesic was administered (i.e. spontaneous breathing was difficult and laboured). Consequently it was elected to avoid sedation during the recovery from anaesthesia. In hindsight, however, it would have been more appropriate to administer a form of analgesia after the mouse had fully

regained consciousness and was back in its housing; a protocol that will be incorporated in future studies. During the subsequent days post-surgery, the welfare of the mouse was monitored by recording body weight, food and water consumption, state of surgical wound healing and observing general appearance and behavior.

2.3. Measurement of heart weight

At the completion of each experiment, each mouse was euthanized by anaesthetic overdose, the heart was excised, the atria were removed, and the right ventricle wall was separated from the left ventricle + septum. Tissues were blotted and weighed. Right and left ventricular weights were expressed as the ratio of the RV to the left ventricular + septum weight (W_{RV}/ $W_{LV + septum}$, Fulton's ratio). The heart mass of an additional five mice that underwent sham surgery was also measured. The sham surgery included a thoracotomy, exposing the right ventricle, and a purse-string suture (7.0 Prolene suture) was fixed to the surface of the ventricle wall. The heart mass of sham mice was measured 1 week after surgery.

2.4. Data acquisition by telemetry

Pulmonary arterial pressure (PAP) was measured in the conscious mouse using the telemetry system (Data Sciences, St. Paul, MN, USA). The components of the radio-telemetry system have previously been described in detail (Hess et al., 1996; Mills et al., 2000). The implantable transmitter (model TA11PA-C20) consisted of a catheter (0.4 mm diameter, 40 mm long) and transducer (~12 mm diameter, 23 mm long) and weighed 3.4 g (Data Sciences have subsequently developed a smaller transmitter model (TA11PA-C10) with a weight of only 1.4 g). The tip of the catheter comprised a biocompatible viscous gel that prevented blood reflux and was coated with an anti-thrombogenic film to inhibit thrombus formation. The transmitter signal was relayed from a receiver platform (RPC-1) to a digitized input that was then continuously sampled at 200 Hz with an 8-channel MacLab/8s interface hardware system (AD Instruments Pty Ltd, Japan Inc.), and recorded on a Macintosh Power Book G4 using Chart (v. 5.0.1, AD Instruments). All transmitters were provider pre-calibrated, although the accuracy of the calibrated signal was confirmed using a mercury manometer to within 1.5 mm Hg immediately prior to implantation. Furthermore, during recording the pressure signal from the transmitter was calibrated in reference to atmospheric pressure (Ambient-Pressure Monitor, C11PR). Heart rate (HR) was derived from the pulmonary arterial systolic peaks.

2.5. Experimental protocol

2.5.1. Baseline
Following recovery from anaesthesia, mice were placed in their housing on top of a telemetric receiver. All operated mice were housed with one other non-operated mouse for the entire duration of the study, except for when each operated mouse was tested with hypoxia and/or L-NAME (see below). The PAP

of five mice was recorded for 8 consecutive days. The PAP of one mouse was recorded for 14 consecutive days.

2.5.2. Acute hypoxia
The PAP response to acute hypoxia (10 min of 8% O_2) was tested in three mice on either day 7 or day 8 post-surgery. On the day of an experiment, the removable top of the mouse's housing was replaced with a modified lid in order to create a sealed chamber (the non-operated companion mouse had been placed in a separate cage for the day). The air-tight housing was then incorporated in a unidirectional flow circuit into which either air or hypoxia was delivered (~1 L/min). When the inlet gas was switched from air to hypoxia, ~3 min was required to flush the housing with the hypoxic gas. Both air and hypoxia were first humidified before delivery to the housing. The hypoxic gas mixture (i.e. 8% O_2) was produced using gas rotameters (O_2 and N_2). Once the mouse was resting quietly, baseline data were collected for approximately 10 min. Data were continuously recorded as the inlet gas was switched from air to 8% O_2, and then for the duration of hypoxic exposure (10 min) and also during the recovery period. If the mouse became agitated or started moving within its housing, the hypoxic test was terminated and then repeated at a later time.

2.5.3. L-NAME
The three mice that were exposed to hypoxia were also injected with the NO synthase inhibitor, N^{ω}-nitro-L-arginine methyl ester (L-NAME, Sigma-Aldrich, St. Louis, MO., USA) (50 mg/kg, s.c.) either on the same day or 1 day after the hypoxia test. Mice had to be removed from their cage in order to receive the injection; therefore, it was not possible to continuously measure PAP. Furthermore, handling of mice incorporated some degree of stress, so when the mouse was placed back in its cage, it spent 1 to 2 min moving within the cage before starting to relax. Consequently, the effect of L-NAME on PAP could not be accurately measured for approximately 3 min after L-NAME had been injected. Data were continuously recorded for 20 min after L-NAME was injected.

2.6. Data analysis

All data were collected while mice were resting (often sleeping) and relatively inactive. Steady-state data were used for obtaining the mean responses to hypoxia (at the 8th minute of hypoxia) and L-NAME (at the 5th minute after injection) presented in graphs. One-way ANOVA (factorial) was used to test for statistical differences between baseline values and the mean responses for hypoxic and L-NAME. A P-value ≤ 0.05 was predetermined as the level of significance for all statistical analysis.

3. Results

3.1. Recovery from surgery

A total of 15 mice underwent surgery. Three of the mice died during surgery due to factors such as the invasiveness

Fig. 1. A photograph of a normal mouse (right) and a mouse with a telemetric transmitter surgically implanted into its abdominal cavity (left). The transmitter catheter is located within the pulmonary artery for the continuous monitoring of pulmonary arterial pressure (PAP). The PAP traces presented in Fig. 2 were obtained from this mouse. The photo was taken 1 week after surgery.

of the surgery and the potential for excessive blood loss. In the early stages of developing the surgical technique, the primary complication of obtaining PAP from conscious mice, related to the positioning of the catheter tip in an otherwise short (~2 mm) and sharply curved pulmonary arterial trunk. In the first seven mice, the tip of the transmitter catheter was displaced from its original position within the first 2 days post surgery so that the catheter tip was within the ventricle. In such instances it was not possible to measure MPAP, although it was still possible to measure ventricular pressure (which can be used as an estimate of PAP). In subsequent mice, it was elected to secure the transmitter catheter to the 4th and 5th rib to prevent withdrawal of the catheter from the pulmonary artery into the ventricle. This addition to the surgery ensured that pulmonary arterial pressure could be consistently recorded in all remaining mice (i.e. $n=5$).

Although operated mice were comparatively immobile for 2 days after surgery, by the third day mice had started to exhibit normal behavioral patterns for a mouse, such as grooming, burrowing within the housing litter and running around the cage. By day 7, the two mice that had the transmitters positioned in the abdominal cavity were indistinguishable in appearances and activeness from a non-operated mouse, and they had regained body weight to within approximately 1 g of its pre-surgery weight (Fig. 1).

3.2. Baseline PAP

In general, we observed that a clear PAP signal could only be recorded while the mouse was relatively inactive (i.e. resting or sleeping). If the mouse began to run or burrow within its housing, the signal was contaminated by artifacts and therefore illegible. Consequently, it was not possible to continuously obtain a clear PAP signal for 24 h/day. Nevertheless, we were able to record a clear baseline PAP signal in each of the five mice at times of rest for 8 consecutive days after surgery. Typical traces of the recorded PAP signal over the 8-day period are presented in Fig. 2A. Generally, within the first week post-surgery, MPAP fluctuated between 19.9 mm Hg (day 3) and 14.1 mm Hg (day 7) (Fig. 2B). The baseline data obtained from the average of days 7 and 8 post-surgery are presented in Table 1. In one mouse, PAP was recorded for an additional 7 days (total of 14 days), and in this period MPAP remained stable (~16.9 mm Hg by day 14), as it had during the first week post-surgery.

The surgical procedure for pulmonary catheterization caused a small, albeit significant, increase ($P<0.05$) in the RV/LV+septum ratio by 1 week post-surgery (Table 1). The small increase in RV/LV+septum ratio was likely due to the
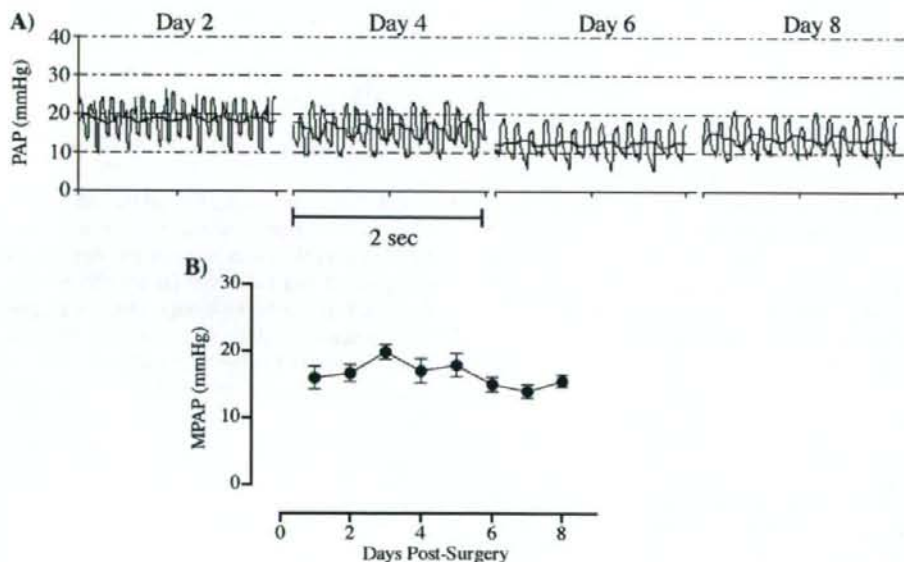

Fig. 2. (A) Example of typical PAP chart traces obtained from a conscious mouse (pictured in Fig. 1) on days 2, 4, 6 and 8 post-surgery. The solid line through the fluctuating PAP trace represents the average PAP. (B) The mean (±S.E.M.) MPAP of five conscious mice recorded each day for 1 week following surgery.

Table 1
Baseline pulmonary arterial pressure and heart mass data of mice

	Transmitter	Sham surgery	No surgery
Mean PAP (mm Hg)	14.9±0.7	N/A	N/A
Systolic PAP (mm Hg)	24±1.2	N/A	N/A
Diastolic PAP (mm Hg)	8.5±0.9	N/A	N/A
HR (bpm)	487±22	N/A	N/A
RV/100 g (mg)	106±5	104±3	94±4
LV+septum/100 g (mg)	278±19	272±11	296±21
RV/LV+septum	0.39±0.01	0.38±0.01	0.32±0.01[†]

Data are presented as mean±S.E.M. [†]Significant difference in RV/LV+septum ratio between mice that did not undergo surgery ($n=5$) and operated mice with ($n=5$) or without (sham—$n=5$) a telemetric transmitter ([†]$P<0.05$).

invasiveness of the surgical procedure (we observed fibrotic tissue surrounding the suture, which was used to anchor the catheter to the wall of the right ventricle), and not due to the presence of a catheter within the pulmonary artery since, (i) sham-operated mice had a similar increase in RV/LV+septum ratio (fibrotic tissue also surrounded the suture) and (ii) there was no increase in baseline pulmonary arterial following the recovery from surgery (an increase in PAP could have increased the workload of the right ventricle provoking right ventricular hypertrophy).

3.3. Pulmonary responses to hypoxia and L-NAME

Three mice were exposed to hypoxia (8% O_2 for 10 min) and, separately, administered L-NAME (50 mg/kg, s.c.) on day 7 or 8 post-surgery. A requisite for collecting data in response to hypoxia and L-NAME was that the mouse remained
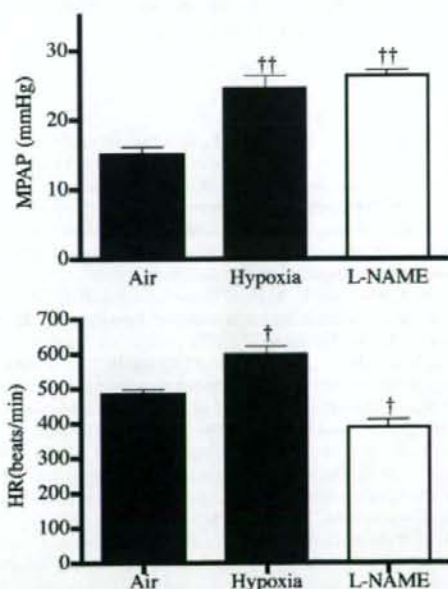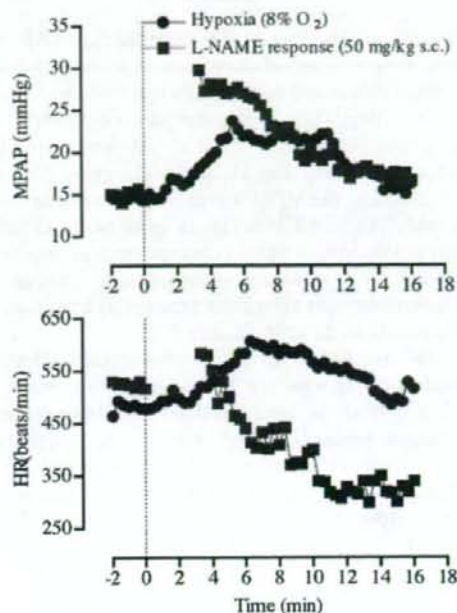

Fig. 4. The transient MPAP and HR responses of a conscious mouse to acute hypoxia (8% O_2 for 10 min) and L-NAME (50 mg/kg, s.c.). Each data point represents the average of a 20-s block of recording. Data could not be recorded while L-NAME was administered, or for the first 3 min after the mouse was placed back into its housing.

relatively still in order to obtain a clear PAP signal during data collection. Subsequently, several attempts were made before clear data could be obtained during hypoxia or after L-NAME administration. The mean data are presented in Fig. 3 and a typical transient PAP response to hypoxia and L-NAME recorded in one mouse is illustrated in Fig. 4.

During hypoxic exposure MPAP gradually increased before stabilizing ~63% above baseline values ($P<0.001$; Fig. 3), which was sustained until the end of hypoxic exposure. Once the inlet gas was switched back to air, MPAP gradually declined, returning to pre-hypoxia values within approximately 5 min (Fig. 4).

L-NAME (50 mg/kg, s.c.) provoked an 86% increase in MPAP ($P<0.001$; Fig. 3) within 5 min of the injection. Subsequently, MPAP gradually declined back towards pre-L-NAME values (Fig. 4). In general, L-NAME provoked a gradual decline in HR (i.e. baroreflex) that continued for the 20-min period of recording (Fig. 4).

4. Discussion

To the best of our knowledge this is the first study to measure pulmonary arterial pressure (PAP) in the conscious, unrestrained mouse. Furthermore, we were also able to measure the changes in PAP in response to the well-known pulmonary stimulants, hypoxia and L-NAME, effectively demonstrating the reliability of using telemetry for recording a variable range of PAP values in the conscious mouse.

Fig. 3. Steady-state MPAP and HR responses to acute hypoxia (8% O_2 for 10 min) and L-NAME (50 mg/kg, s.c.) in conscious mice. Data ($n=3$) are presented as mean±S.E.M. [†]Significantly different from baseline (i.e. air) values ([†]$P<0.01$; [††]$P<0.001$).

Although no other study has reported the PAP of the conscious mouse, some studies have measured PAP in the anaesthetized mouse and subsequently reported a wide range of MPAP values, depending on whether an open-chest (12.8 ± 1.9 mm Hg, Champion et al., 2000) or closed-chest preparation is used (16.4 to 20.3 mm Hg, Steudel et al., 1997; Zhao et al., 1999). Regardless, the MPAP reported in the conscious mouse of this study (14.9 ± 0.7 mm Hg) is more likely to reflect a 'true' physiological state of the pulmonary vasculature, without the influence of a ventilator or anaesthesia. Campen et al. (2005) monitored right ventricular pressure in conscious mice, but were unable to directly measure PAP.

We monitored MPAP for 8 days after surgery, although we confirmed in one mouse that the PAP signal was stable for 2 weeks and is likely to have remained recordable for considerably longer periods. Indeed, the use of telemetry has previously been validated and shown to provide reliable physiological results (arterial BP) in conscious mice for up to 150 days (Butz & Davisson, 2001; Mills et al., 2000). Therefore, an important advantage arising from this study is the ability to accurately monitor and measure changes in pulmonary vascular modulation during mid-term to long-term studies that involve, for example, pharmaceutical intervention.

The primary limitation of this study is the inability to clearly record MPAP in an over-active mouse. All measurements were taken during the day, when the mouse, a nocturnal rodent, was relatively inactive (e.g. slow walking, eating, resting or sleeping). Therefore data were relatively easy to obtain. However, when attempts were made to collect data overnight, when mice were fully active, the PAP signal often became incomprehensible. This limitation would most likely apply to studies aiming to investigate, for example, pulmonary dynamics during exercise.

There are two main factors that may account for this observed complication. Firstly, it may be due to the presence of a catheter (OD of 0.4 mm) within a very short and sharply curved pulmonary arterial trunk. When the tip was accurately position within the pulmonary artery, any slight forward shift of the catheter (>1.0 mm), such as the mouse running, caused the tip to hit the arterial wall. Secondly, the most likely reason we could not continuously record PAP may be due to signal 'noise' or 'artifacts' generated due to abrupt movement of the transmitter body within the abdomen or on the mouse's back—a common problem observed with the use of telemetry. Recently, Data Sciences developed a considerably smaller transmitter model (TA11PA-C10—weight of 1.4 g) that can fit comfortably within the abdomen of an adult mouse. Therefore, any abrupt movements of the smaller transmitter are less likely to cause illegible noise that is commonly seen when the larger transmitter (i.e. model TA11PA-C20) is placed subcutaneously on the mouse's back.

It has been well documented that both acute hypoxia and the NOS inhibitor L-NAME can cause, via independent mechanisms, vasoconstriction of the pulmonary vasculature, ultimately causing an increase in PAP. The results of our study using the conscious mouse concur with this generally accepted concept. We reported that 8% O_2 induced a 63% increase in MPAP. These results appear more robust than that of the anaesthetized mouse reported by Champion et al. (2000), although their study used a more mild level of hypoxia (~34% increase in MPAP in response to 10% O_2). Similarly, we reported that 50 mg/kg L-NAME (s.c.) provoked an 86% increase in MPAP, which is somewhat larger than that reported for the anaesthetized mouse using the same dose (30% increase in MPAP, Champion et al., 2000). However, Champion et al. (2000) noted that NOS inhibition (using L-NAME) was more effective at provoking vasoconstriction when flow-rate (i.e. cardiac output) was high. Since anaesthesia depresses baseline cardiorespiratory variables and their responses to certain stimulants, the cardiac output of the conscious mouse is likely to be greater than that of the anaesthetized mouse and, therefore, be more susceptible to the inhibition of endothelial NOS by L-NAME. Furthermore, the actual responsiveness of the vasculature to L-NAME is likely to be more robust without the depressive effects of anaesthesia.

In summary, we have demonstrated the ability to measure PAP (including sPAP and dPAP) and HR by telemetry in conscious, unrestrained mice. Despite some limitations of this study, one of the most important advantages is the possibility to monitor and record the transient effects of cardioactive compounds, in normal or genetic 'knockout' mice, without anaesthesia or without the stress that results from more conventional indwelling-catheter techniques.

References

Ao, Q., Huang, L., Zhu, P., Xiong, M., & Wang, D. (2004). Inhibition of expression of hypoxia-inducible factor-1alpha mRNA by nitric oxide in hypoxic pulmonary hypertension rats. *Journal Huazhong University of Science and Technology Medical Sciences, 24*, 5–8.

Butz, G. M., & Davisson, R. L. (2001). Long-term telemetric measurement of cardiovascular parameters in awake mice: A physiological genomics tool. *Physiological Genomics, 5*, 89–97.

Campen, M. J., Shimoda, L. A., & O'Donnell, C. P. (2005). The acute and chronic cardiovascular effects of intermittent hypoxia in C57BL/6J mice. *Journal of Applied Physiology, 7*.

Champion, H. C., Villnave, D. J., Tower, A., Kadowitz, P. J., & Hyman, A. L. (2000). A novel right-heart catheterization technique for in vivo measurement of vascular responses in lungs of intact mice. *American Journal of Physiology. Heart and Circulatory Physiology, 278*, H8–H15.

Fagan, K. A., Fouty, B. W., Tyler, R. C., Morris, Jr., K. G., Hepler, L. K., Sato, K., et al. (1999). The pulmonary circulation of homozygous or heterozygous eNOS-null mice is hyperresponsive to mild hypoxia. *Journal of Clinical Investigation, 103*, 291–299.

Fagan, K. A., Tyler, R. C., Sato, K., Fouty, B. W., Morris, Jr., K. G., , Huang, P. L., et al. (1999). Relative contributions of endothelial, inducible, and neuronal NOS to tone in the murine pulmonary circulation. *American Journal of Physiology. Lung Cellular and Molecular Physiology, 277*, L472–L478.

Hampl, V., Archer, S. L., Nelson, D. P., & Weir, E. K. (1993). Chronic EDRF inhibition and hypoxia: Effects on pulmonary circulation and systemic blood pressure. *Journal of Applied Physiology, 75*, 1748–1757.

Hampl, V., Tristani-Firouzi, M., Nelson, D. P., & Archer, S. L. (1996). Chronic infusion of nitric oxide in experimental pulmonary hypertension: Pulmonary pressure-flow analysis. *European Respiratory Journal, 9,* 1475–1481.

Hess, P., Clozel, M., & Clozel, J. P. (1996). Telemetry monitoring of pulmonary arterial pressure in freely moving rats. *Journal of Applied Physiology, 81,* 1027–1032.

Huang, K. L., Wu, C. P., Kang, B. H., & Lin, Y. C. (2002). Chronic hypoxia attenuates nitric oxide-dependent hemodynamic responses to acute hypoxia. *Journal of Biomedical Science, 9,* 206–212.

Li, D., Laubach, V. E., & Johns, R. A. (2001). Upregulation of lung soluble guanylate cyclase during chronic hypoxia is prevented by deletion of eNOS. *American Journal of Physiology. Lung Cellular and Molecular Physiology, 281,* L369–L376.

Mills, P. A., Huetteman, D. A., Brockway, B. P., Zwiers, L. M., Gelsema, A. J., Schwartz, R. S., et al. (2000). A new method for measurement of blood pressure, heart rate, and activity in the mouse by radiotelemetry. *Journal of Applied Physiology, 88,* 1537–1544.

Quinlan, T. R., Li, D., Laubach, V. E., Shesely, E. G., Zhou, N., & Johns, R. A. (2000). eNOS-deficient mice show reduced pulmonary vascular proliferation and remodeling to chronic hypoxia. *American Journal of Physiology. Lung Cellular and Molecular Physiology, 279,* L641–L650.

Steudel, W., Ichinose, F., Huang, P. L., Hurford, W. E., Jones, R. C., Bevan, J. A., et al. (1997). Pulmonary vasoconstriction and hypertension in mice with targeted disruption of the endothelial nitric oxide synthase (NOS 3) gene. *Circulation Research, 81,* 34–41.

Tank, J., Jordan, J., Diedrich, A., Obst, M., Plehm, R., Luft, F. C., et al. (2004). Clonidine improves spontaneous baroreflex sensitivity in conscious mice through parasympathetic activation. *Hypertension, 43,* 1042–1047.

Van Vliet, B. N., Chafe, L. L., & Montani, J. P. (2003). Characteristics of 24 h telemetered blood pressure in eNOS-knockout and C57Bl/6J control mice. *Journal of Physiology, 549,* 313–325.

Weissmann, N., Winterhalder, S., Nollen, M., Voswinckel, R., Quanz, K., Ghofrani, H. A., et al. (2001). NO and reactive oxygen species are involved in biphasic hypoxic vasoconstriction of isolated rabbit lungs. *American Journal of Physiology. Lung Cellular and Molecular Physiology, 280,* L638–L645.

Xue, B., Pamidimukkala, J., & Hay, M. (2005). Sex differences in the development of angiotensin II-induced hypertension in conscious mice. *American Journal of Physiology. Heart and Circulatory Physiology, 288,* H2177–H2184.

Zhao, L., Long, L., Morrell, N. W., & Wilkins, M. R. (1999). NPR-A-deficient mice show increased susceptibility to hypoxia-induced pulmonary hypertension. *Circulation, 99,* 605–607.

Crystal structures of VAP1 reveal ADAMs' MDC domain architecture and its unique C-shaped scaffold

Soichi Takeda[1,2,*], Tomoko Igarashi[1], Hidezo Mori[1] and Satohiko Araki[3]

[1]Department of Cardiac Physiology, National Cardiovascular Center Research Institute, Suita, Osaka, Japan, [2]Laboratory for Structural Biochemistry, Riken Harima Institute at SPring-8, Mikazuki, Sayo, Hyogo, Japan and [3]Sugashima Marine Biological Laboratory, Graduate School of Science, Nagoya University, Toba, Mie, Japan

ADAMs (a disintegrin and metalloproteinase) are sheddases possessing extracellular metalloproteinase/disintegrin/cysteine-rich (MDC) domains. ADAMs uniquely display both proteolytic and adhesive activities on the cell surface, however, most of their physiological targets and adhesion mechanisms remain unclear. Here for the first time, we reveal the ADAMs' MDC architecture and a potential target-binding site by solving crystal structures of VAP1, a snake venom homolog of mammalian ADAMs. The D-domain protrudes from the M-domain opposing the catalytic site and constituting a C-shaped arm with cores of Ca^{2+} ions. The disintegrin-loop, supposed to interact with integrins, is packed by the C-domain and inaccessible for protein binding. Instead, the hyper-variable region (HVR) in the C-domain, which has a novel fold stabilized by the strictly conserved disulfide bridges, constitutes a potential protein–protein adhesive interface. The HVR is located at the distal end of the arm and faces toward the catalytic site. The C-shaped structure implies interplay between the ADAMs' proteolytic and adhesive domains and suggests a molecular mechanism for ADAMs' target recognition for shedding.

Introduction

ADAMs (a disintegrin and metalloproteinase) or MDC (metalloproteinase/disintegrin/cysteine-rich) proteins comprise an emerging class of mammalian metalloproteinases with potential regulatory roles in cell–cell and cell–matrix adhesion and signalling (Becherer and Blobel, 2003; Seals and Courtneidge, 2003; White, 2003; Blobel, 2005). To date, over 30 ADAMs have been identified in a variety of species from fission yeast to human. Roughly, half of these are believed to

*Corresponding author. Department of Cardiac Physiology, National Cardiovascular Center Research Institute, Fujishirodai 5-7-1, Suita, Osaka, 565-8565, Japan. Tel.: +81 6 6833 5012 ext.2381; Fax: +81 6 6872 7485; E-mail: stakeda@ri.ncvc.go.jp

function as active metalloproteinases and thus to constitute major membrane-bound sheddase that can proteolytically release cell-surface-protein ectodomains including growth factors and cytokines, their receptors and cell adhesion molecules. For example, ADAM17 (TACE, TNF-α converting enzyme) releases many cell-surface proteins including TNF-α precursor (Black *et al*, 1997; Moss *et al*, 1997) and ADAM10 (kuzbanian), which dictates lateral inhibition of *Drosophila* neurogenesis (Rooke *et al*, 1996), releases Notch ligand Delta (Qi *et al*, 1999) and Notch itself (Pan and Rubin, 1997). With regard to cellular interactions, fertilin α and β (ADAM1 and ADAM2, respectively) have been identified as sperm surface molecules essential for fertilization (Primakoff *et al*, 1987; Blobel *et al*, 1990, 1992) and meltrin α (ADAM12) is implicated in myogenesis (Yagami-Hiromasa *et al*, 1995). ADAMs have been associated with numerous diseases including arthritis, Alzheimer's disease, and cancer (Duffy *et al*, 2003; Moss and Bartsch, 2004). ADAM33 has been genetically linked with asthma (Van Eerdewegh *et al*, 2002). ADAMs uniquely display both proteolytic and adhesive activities on the cell surface, however, most of their physiological targets and the adhesion mechanisms remain unclear.

Disintegrins are small proteins (40–90 aa) isolated from snake venom typically with an Arg-Gly-Asp (RGD) recognition sequence on an extended loop (disintegrin-loop) that inhibit platelet aggregation via integrin binding (Huang *et al*, 1987; Calvete *et al*, 2005). ADAMs are unique among cell surface proteins in possessing a disintegrin (D-) domain and thus it has been suggested that integrins might be common receptors for ADAMs (Blobel *et al*, 1992; Evans, 2001; White, 2003). However, the RGD sequence in the ADAMs' disintegrin-loop is usually replaced by XXCD and therefore, its adhesive potential has been controversial. Both the ADAMs' D- and cysteine-rich (C-) domains are involved in the protein–protein interactions (Myles *et al*, 1994; Almeida *et al*, 1995; Zolkiewska, 1999; Iba *et al*, 2000; Gaultier *et al*, 2002; Smith *et al*, 2002), however, the details of the interactions have remained elusive. This is because high-resolution structures have been available only for isolated domains (Maskos *et al*, 1998; Orth *et al*, 2004; Janes *et al*, 2005) and no structural information has been available for the C-domain of the canonical ADAMs. To clarify the molecular mechanisms of target recognition for shedding by and of cellular adhesion via ADAMs, elucidation of the atomic structure of the ADAMs' MDC domains is indispensable.

To obtain structural data on an ADAM family member, we exploited the fact that hemorrhagic P-III snake venom metalloproteinases (SVMPs) share the ADAMs' MDC architecture (Jia *et al*, 1996; Evans, 2001; Fox and Serrano, 2005). Most ADAMs possess additionally, EGF-like, transmembrane and cytoplasmic domains and therefore are primarily membrane-associated, whereas SVMPs are secreted. Vascular apoptosis-inducing protein-1 (VAP1) is a disulfide-bridged

homodimer P-III SVMP isolated from *Crotalus atrox* venom (Masuda *et al*, 1998, 2000). VAP1's stability and intrinsic two-fold symmetry enabled us to solve the crystal structures at 2.5-Å resolution. The structure reveals the residues that are important for stabilizing the MDC architecture are strictly conserved throughout the primary structure among all the known ADAMs. Therefore, the present structure represents the general architecture of ADAMs' MDC domains and provides insights into the molecular mechanism of the ADAMs' target recognition.

Results

Structure determination

VAP1 yielded crystals readily, and initial phases were determined by molecular replacement method using the structure of P-I SVMP, acutolysin-C (1QUA) (Zhu *et al*, 1999) as a starting model. Although the initial model, with 99 identical residues out of 197, represented less than 50% of the total molecule, two distinct local noncrystallographic two-fold symmetry (NCS) operations (see below) allowed us to completely model the whole molecule. The native structures were determined from the crystals with two distinct space groups, $P2_12_12_1$ and $P4_12_12$, both at 2.5-Å resolution (Table I).

Orthorhombic crystals were used for inhibitor soaking and the GM6001 ((3-(*N*-hydroxycarboxamido)-2-isobutyl-propanoyl-Trp-methylamide))-bound structure was determined at 3.0-Å resolution (Table I). In either crystal forms, the asymmetric unit contained one dimer molecule. The four monomers in the two crystal forms have almost identical structures, except for slight variations in their domain orientations, terminal residues, surface loops and active-site GM6001-binding region.

MDC architecture

The MDC architecture of VAP1 is shown in Figure 1A and B. The metalloproteinase (M-) domains in the dimer are related by NCS such that their active sites point in opposite directions and an intermolecular disulfide bridge is formed between symmetry-related Cys365 residues (Figure 1A). The M-domain is followed by a disintegrin (D-) domain that is further divided into D_s- and D_a-domains (see below). The D_s-domain protrudes from the M-domain close to the Ca^{2+}-binding site I (see below) opposing the catalytic site. The D-domain forms a C-shaped arm, together with the cysteine-rich (C-) domain, with its concave surface toward the M-domain. There are no direct interactions between the arm and the M-domain. Notably, the distal portion of the C-domain comes close to

Table I Data collection and refinement statistics

	Native (orthorhombic)	Native (tetragonal)	GM6001-bound
Data collection			
Space group	$P2_12_12_1$	$P4_12_12$	$P2_12_12_1$
Cell dimensions			
a, b, c (Å)	86.7, 93.3, 137.7	93.9,93.9,244.8	86.3, 91.4, 136.0
α, β, γ (deg)	90, 90, 90	90, 90, 90	90, 90, 90
Resolution (Å)	50–2.50 (2.59–2.50)	50–2.50 (2.59–2.50)	50–2.95 (3.06–2.95)
R_{merge}[a]	0.072 (0.369)	0.084 (0.380)	0.072 (0.367)
$I/\sigma I$	14.4 (2.9)	18.7 (7.1)	12.6 (4.3)
Completeness (%)	99.4 (98.8)	99.7 (99.6)	99.9 (99.4)
Redundancy	3.91	12.7	4.95
Refinement			
Resolution (Å)	50–2.50 (2.59–2.50)	50–2.50 (2.59–2.50)	50–2.95 (3.06–2.95)
No. of reflections	38874	38786	23295
R_{work}[b]$/R_{free}$[c]	0.212/0.258	0.229/0.269	0.208/0.264
No. of atoms			
Protein	6558	6513	6558
Zn^{2+}	2	2	2
Ca^{2+}	4	4	4
Co^{3+}	1		1
N-acetyl glucosamine	56	42	56
GM6001			56
Water	205	165	35
B-factors			
Protein	44.9	51.2	55.4
Zn^{2+}	40.9	41.6	46.4
Ca^{2+}	43.5	52.4	49.3
Co^{3+}	35.5		56.8
N-acetyl glucosamine	69.8	65.1	75.8
GM6001			78.6
Water	39.8	41.5	37.0
R.m.s deviations			
Bond lengths (Å)	0.0052	0.0080	0.0038
Bond angles (deg)	1.18	1.39	0.92

[a]$R_{merge} = \sum_{hkl}\sum_i |I_i(hkl) - <I (hlk)>| / \sum_{hkl}\sum_i I_i(hkl)$, where $I_i(hkl)$ is the *i*th intensity measurement of reflection *hkl* and $\langle I(hlk) \rangle$ is its average.
[b]$R_{work} = \sum (||F_{obs}| - |F_{calc}|| / \sum |F_{obs}|$.
[c]$R_{free} = R$-value for a randomly selected subset (5%) of the data that were not used for minimization of the crystallographic residual.
Highest resolution shell is shown in parenthesis.
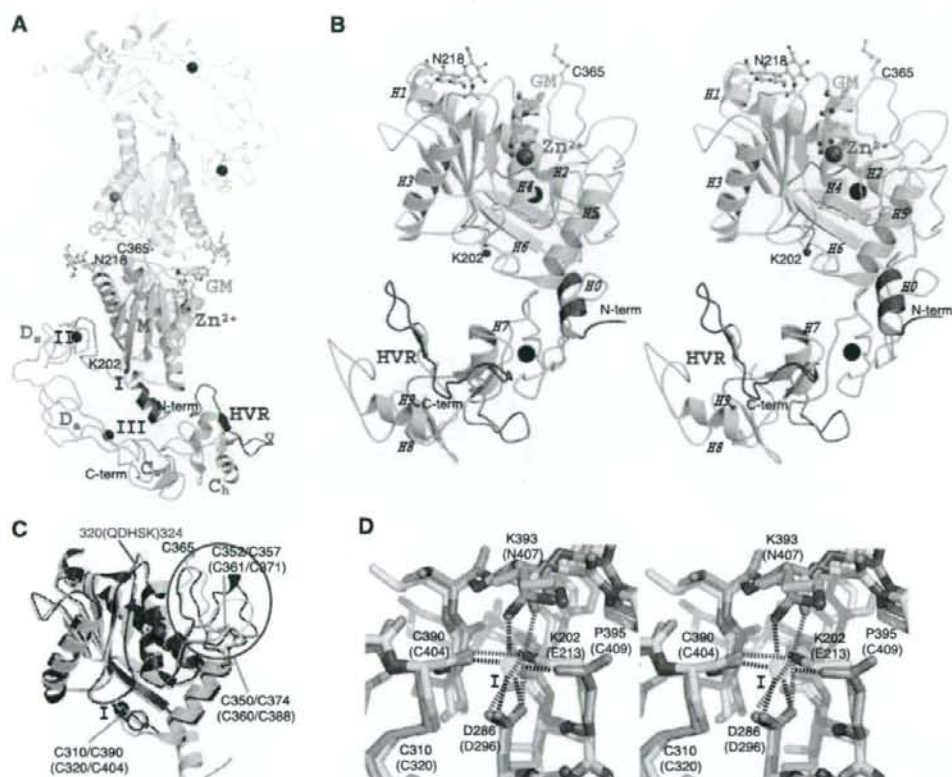For each data set, single crystal was used for measurement.

Figure 1 MDC architecture. (**A**) VAP1 dimer viewed from the NCS axis. The H0-helix, M-domain, linker, D_s-, D_a-, C_w-, and C_h-domains and HVRs belonging to the one monomer are shown in red, yellow, gray, cyan, pink, gray, green and blue, respectively. The disulfide-linked counterpart is shown in gray. Zinc and calcium ions are represented as red and black spheres, respectively. The NAG (*N*-acetyl-glucosamine, in orange) moieties linked to Asn218, the calcium-mimetic Lys202 and the bound inhibitor GM6001 (GM, in green) are in ball-stick representations. (**B**) Stereo view of VAP1 monomer from the direction nearly perpendicular to (A). The helix numbers are labelled. (**C**) Superposition of the M-domains of ADAM33 (blue) and VAP1 (yellow). The calcium ion bound to site I and the zinc ion in ADAM33 are represented by black and red spheres, respectively. The disulfide bridges are indicated in black and blue letters for VAP1 and ADAM33, respectively. The QDHSK sequence for the dimer interface in VAP1 (residues 320–324) is in red. (**D**) Comparison of the calcium-binding site I structures of ADAM33 (blue) and VAP1 (yellow) *in stereo*. The residues in ADAM33 and in VAP1 are labelled in blue and black, respectively. A calcium ion and a water molecule bound to ADAM33 are represented as green and red spheres, respectively. The ammonium group of Lys202 in VAP1 occupies the position of the calcium ion in ADAM33. In ADAM33 (Orth *et al*, 2004), side-chain oxygen atoms of Glu213, Asp296 and Asn407, the carbonyl oxygen of Cys404 and a water molecule form the corners of a pentagonal bipyramid and ligand to the calcium ion.

and faces toward the catalytic site in the M-domain. The C-terminus Tyr610 is located proximal to the boundary between the D_a- and C-domains (Figure 1A and B). Aside from Cys365, each monomer contains 34 cysteinyl residues, all of which are involved in disulfide bonding, and their spacings are strictly conserved among ADAMs (Figure 2 and Supplementary Figure 1) except within the substrate-binding (between the helices H4 and H5) and the HVR (see below) regions. Figure 2 provides a selected subset of the sequence alignments and the entire alignments of VAP1 and 39 ADAM sequences, including all 23 human ADAMs so far available, can be found as Supplementary Figure 1.

M-domain

Each VAP1 M-domain corresponds to a very similar structure to that of ADAM33 (Orth *et al*, 2004), with a flat ellipsoidal shape having a central core made up of five stranded β-sheets and five α-helices and a conserved methionine (Met-turn)

below the active site histidine residues, which bears the typical structural feature of metzincin family of metalloproteinases (Bode *et al*, 1993). However, they differ in the dimer interface and the loop structure around the substrate-binding site (Figure 1C) that corresponds to the variable region in the primary structure (between the helices H4 and H5, see Figure 2). The N-terminal helix (H0) is also unique in VAP1. The dimer interface is best characterized by the recognition sequence QDHSK (residues 320–324, see Figure 1C and Supplementary Figure 2A–C) and by Cys365, however these are not conserved among ADAMs; therefore, none of the ADAMs' M-domains are suggested to form a stable dimer as VAP1. A peptide-like hydroxamate inhibitor GM6001 binds to VAP1 (Figure 1A and B, and Supplementary Figure 2D and E) in exactly the same manner as in the marimastat-ADAM33 M-domain complex (Orth *et al*, 2004), suggesting that the catalytic sites of VAP1 and ADAM33 share a common substrate recognition mechanism. The ADAM33
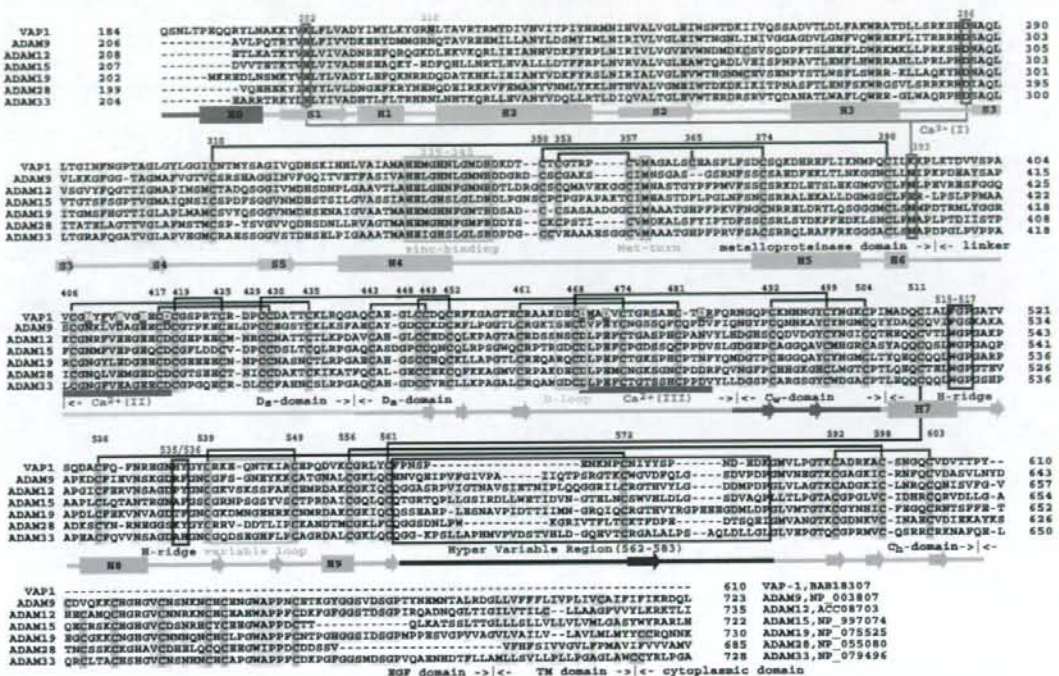
-632-

Figure 2 Sequence alignments of VAP1 and human ADAMs. The cysteinyl residues and the conserved residues are shaded in pink and yellow, respectively. Disulfide bridges, secondary structures and domains are drawn schematically. The HVR, calcium-binding site I, catalytic site and disintegrin-loop (D-loop) are boxed in blue, red, green and cyan, respectively. The hydrophobic ridges (H-ridges) are indicated. Calcium-binding sites II and III and the coordinating residues (shaded in red) are indicated. The NCBI accession numbers for the sequences are indicated.

M-domain structure suggests that most ADAMs have a Ca^{2+}-binding site (designated Ca^{2+}-binding site I) opposing the active-site cleft; however, in VAP1, the distal ammonium group of Lys202 substitutes for the Ca^{2+} ion (Figure 1D). Replacement of the calcium-coordinating glutamate residue with lysine also occurs in ADAM16, ADAM25 and ADAMs38–40 (Supplementary Figure 1).

C-shaped arm

The D-domain follows the M-domain, with a short linker that allows slightly variable domain orientations at V405 as a pivotal point (Figure 3C). The D-domain is further divided into two structural subdomains (Figure 3), the 'shoulder' (D_s-domain, residues 396–440) and the 'arm' (D_a-domain, residues 441–487). The D_s- and D_a-domains constitute a continuous C-shaped arm, together with the following N-terminus region of the C-domain which we designate the 'wrist' (C_w-domain, residues 488–505). There are three disulfide bonds in the D_s-domain, three in the D_a-domain and one in the C_w-domain. The subdomains are connected by single disulfide bridges (Figures 2 and 3A) with slightly variable angles (Figure 3B).

Both the D_s- and D_a-domains contain structural calcium-binding sites. In the D_s-domain, the side-chain oxygen atoms in residues Asn408, Glu412, Glu415 and Asp418, and the carbonyl oxygen atoms of Val405 and Phe410 are involved in pentagonal bipyramidal coordination and constitute Ca^{2+}-binding site II (Figures 2 and 3A). Notably, these residues are

strictly conserved among all known ADAMs (Supplementary Figure 1). However, the side-chain oxygens of Asp469, Asp472 and Asp483, and carbonyl oxygens of Met470 and Arg484 form the corners of a pentagonal bipyramid to the calcium ligand and constitute the D_a-domain Ca^{2+}-binding site III (Figures 2 and 3A) and these residues are highly conserved among ADAMs except ADAM10 and ADAM17 (Supplementary Figure 1). Because of the few secondary-structural elements, bound calcium ions and the disulfide bridges are essential for the structural rigidity of ADAM's C-shaped arm. The RGD-containing disintegrin trimestatin (Fujii et al, 2003) has a similar structure with the D_a-domain (r.m.s.d of 1.24 Å, Figure 3B); however, no disintegrins have been shown to bind Ca^{2+} ions.

Using isolated D-domains or portions thereof, numerous ADAMs and P-III SVMPs have been shown to interact specifically with particular integrins (Evans, 2001; White, 2003; Calvete et al, 2005). However, the disintegrin-loop is packed against the C_w-domain and a disulfide bridge (Cys468–Cys499) further stabilizes the continuous structure (Figure 3A). Therefore, the disintegrin-loop is inaccessible for protein binding.

Hand domain

The 'hand' domain (C_h-domain, residues 505–610) follows the C_w-domain. The C_h-domain, together with the C_w-domain, constitutes a novel fold (Figure 4A). In either crystal form, VAP1 dimers interact with molecules of neighboring
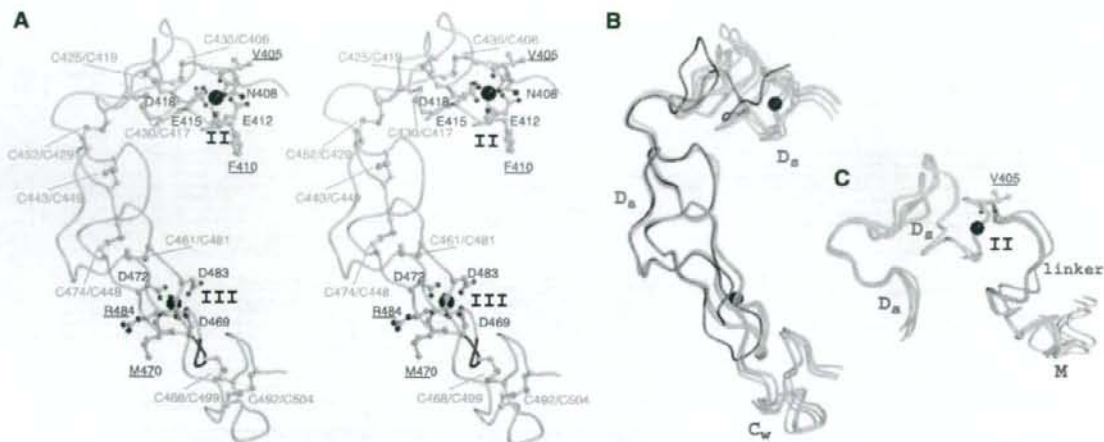
Figure 3 Arm structure. (**A**) Arm structure *in stereo*. The D_s-, D_a-, and C_w-domains are in cyan, pink and light green, respectively. The calcium-coordinating residues and the disulfide bridges are shown in red and green, respectively. The residues with carbonyl oxygen atoms involved in calcium coordination are underlined. Calcium ions are represented as black spheres. The disintegrin-loop (DECD) is in blue. (**B**) Superimposition of the four D_a-domains of VAP1 and trimestatin (1J2L). Trimestatin and its RGD loop are shown in red and blue, respectively. (**C**) Superimposition of the four D_s-domains. The linker between the M- and D_s-domains is shown in gray. Val405 at the pivotal point is indicated.
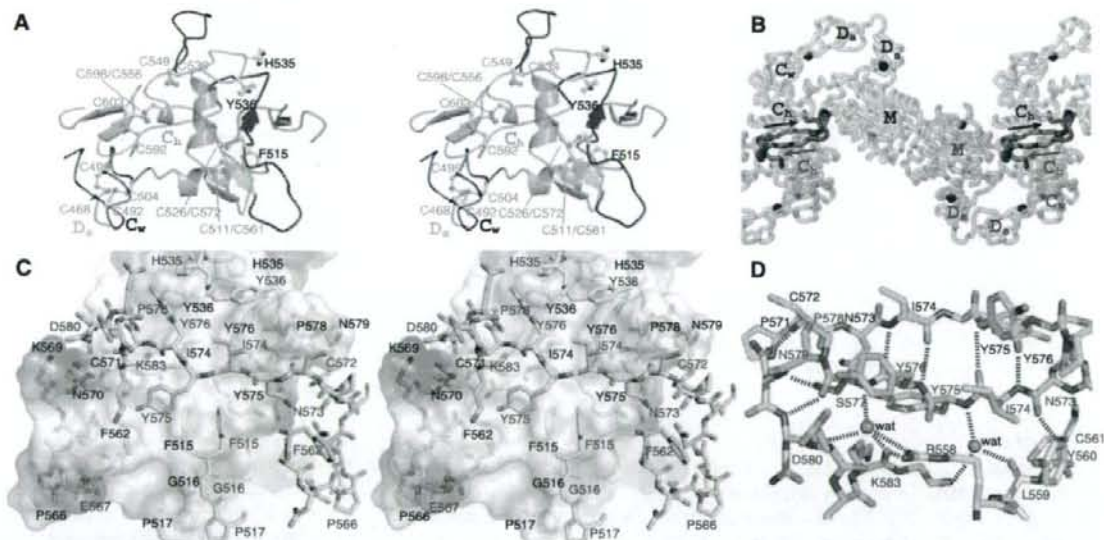

Figure 4 C-domain architecture and HVR. (**A**) The C-domain architecture *in stereo*. The C_w- and C_h-domains are in gray and light green, respectively. The disulfide bridges and the residues forming the hydrophobic ridges are indicated. The HVR and its NCS counterpart are shown in red and blue, respectively. The variable loop (residues 539–549), flanked by two adjacent cysteine residues, is in green. (**B**) Crystal packing in the orthorhombic crystal. The crystallographically equivalent molecules (HVRs) are in cyan (blue) and pink (red), respectively. The arrows indicate the directions of the HVR chains. Zinc and calcium ions are represented as red and black spheres, respectively. (**C**) Interactions between the HVRs (cyan and pink) *in stereo*. The molecular surface of the cyan molecule is shown with the electrochemical surface potential (red to blue). The residues constituting the hydrophobic ridges are in yellow. The residues are labelled in blue and red for cyan and pink, respectively. (**D**) Water-mediated hydrogen-bond network in the HVR. The HVR residues are in pink and cyan; non-HVR residues in the pink molecule are in gray.

units through the C_h-domains such that the molecules form a handshake (Figure 4B). Each C_h-domain interacts with its counterpart through a relatively large complementary surface of 860 Å^2 forming another NCS at the center, although VAP1 exists as dimers, not as oligomers, and is mono-dispersed in solution (data not shown).

HVR as a potential adhesive interface

C_h-domain residues 562–583 are predominantly involved in the handshake (Figure 4B). This is the region in which the ADAM sequences are most divergent and variable in length (16–55 aa) (Figure 2 and Supplementary Figure 1). We have designated this as the hyper-variable region (HVR). The HVR

is subdivided into two structural elements. The N-terminal portion (residues 562–572) fits into an extended loop, filling the gap between the M-domain and the neighboring molecule's C_h-domain and thus fixing the position of the arm (Figure 4B). The variable structures and less-specific interactions suggest that this loop is stabilized by crystal packing. Some ADAMs possess a putative fusion peptide in this segment typical of viral fusion proteins (Blobel et al, 1992; Yagami-Hiromasa et al, 1995), although their role in the actual fusion process has not been demonstrated. However, the remainder of the HVR (residues 572–583) interacts extensively with its counterpart by forming an antiparallel β strand at the center (Figure 4C and D). Although the ability to form β strand is predictable from the sequence, this β strand is stabilized mainly by interchain interactions (Figure 4D). There are no intrachain hydrogen bonds between residues 574–577 and the remainder of the C_h-domain; however a water-mediated hydrogen-bond network stabilizes this segment (Figure 4D). Therefore, it appears, that this β strand might be formed by the induced-fit mechanism upon the association of the C_h-domains and that the conserved disulfide bond (Cys526–Cys572, see Figure 4D) may stabilize the structure when the HVRs are isolated in solution. In addition to the main-chain hydrogen bonds, side-chain atoms (particularly residues I574, Y575, Y576 and P578) in the HVR β strand contribute numerous von der Waals interactions with their counterparts. Aside from the HVR, aromatic residues located at both sides of the β strand in close proximity to the NCS axis create additional interaction surfaces: residues Phe515, Gly516, His535 and Tyr536 in the loop regions form hydrophobic ridges that fit complementarily into the NCS region (Figure 4C). The hydrophobic ridges are highly conserved among ADAMs (Figure 2 and Supplementary Figure 1), thus, in part, they may also constitute binding surfaces.

Discussion

The VAP1 structures reveal highly conserved structural calcium-binding sites and the numbers and the spacings of cysteinyl residues that are essential for maintaining structural rigidity and spatial arrangement of the ADAMs' MDC domains. The C-shaped MDC architecture implies meaningful interplay between the domains and their potential roles in physiological functions.

The HVR creates a novel interaction interface in collaboration with the conserved hydrophobic ridges. Different ADAMs have distinct HVR sequences, which result in distinct surface features, thus, they may function in specifying binding proteins. The HVR is at the distal end of the C-shaped arm and points toward the M-domain catalytic site, with a distance of ~4 nm in between them. Collectively, these observations suggest that the HVR captures the target or associated protein that is processed by the catalytic site (Figure 5). The disintegrin portion is located opposit to and apart from the catalytic site and, thus, might play a primary role as a scaffold that allocates these two functional units spatially. The C-shaped structure also implies how the ADAMs' C-domains cooperate with their M-domains (Reddy et al, 2000; Smith et al, 2002). In membrane-bound ADAMs, the EGF-like domain (~60 aa) follows the C_h-domain (Figure 2) and presumably works as a rigid spacer connecting the MDC-domains with and orientating against the membrane-span-
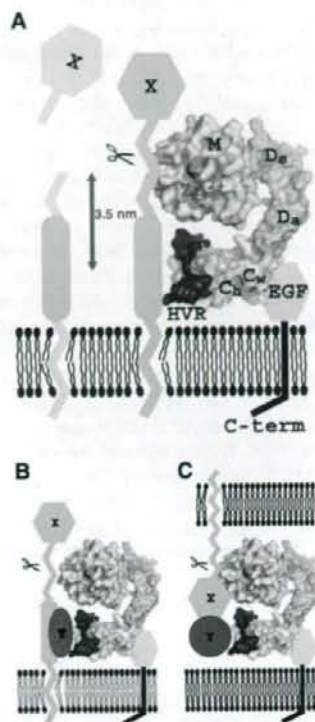

Figure 5 Models for ADAM's shedding. The molecular surface of the VAP1 monomer, without VAP1's unique H0-helix, are colored as in Figure 1A. Hydrophobic ridges are in yellow. EGF-like, transmembrane and cytoplasmic domains are represented schematically. (A) Membrane-anchored substrate molecule 'X' is directly recognized and captured by the HVR on the membrane-bound ADAM molecule. The distance between the center of the HVR (Tyr575) and the catalytic zinc ion is about 3.5 nm. (B) Substrate 'X' is recognized by the ADAM HVR via binding with an associated protein 'Y'. (C) ADAM cleaves substrate 'X' in *trans* via binding with an associated protein 'Y'.

ning region (Figure 5A). Many ADAMs are proteolytically inactive (because of the defects in the catalytic HEXXHXXGXXHD sequence or the post-translational removal of the M-domain), and several of these are important developmentally. Therefore, the HVR may also work to modulate cell–cell and cell–matrix interactions. There is some experimental evidence for C-domain-mediated adhesion. Peptides encompassing the HVR and the hydrophobic ridge from P-III SVMPs interfere with platelet interaction and collagen binding (Kamiguti et al, 2003). A recombinant atrolysin-A C-domain specifically binds collagen I and von Willebrand factor (vWF) and blocks collagen–vWF interaction (Jia et al, 2000; Serrano et al, 2005). ADAM12 interacts with cell-surface syndecan through its C-domain and mediates integrin-dependent cell spreading (Iba et al, 2000). The D/C-domain portion of ADAM13 binds to the ECM proteins laminin and fibronectin (Gaultier et al, 2002). However, most of these studies do not assign specific regions of the C-domain to these interactions and the molecular recognition mechanisms are to be elucidated.

ADAM10 and ADAM17 lack the Ca^{2+}-binding site III and show less sequence similarities in the C-domain with other

canonical ADAMs (Supplementary Figure 1). Comparison of the recently solved ADAM10 D/C-domain partial structure (ADAM10$_{D+C}$) (Janes *et al*, 2005) and that of VAP1 reveals that the atypical ADAM10 shares the continuous D$_a$/C$_w$ structure and the C$_h$-domain scaffold with VAP1; however, it has an disordered D$_s$-domain and an alternate HVR structure and a different orientation between C$_w$- and C$_h$-domains (Figure 6). The locations of four of the five disulfide bridges within the C$_h$-domain are conserved between VAP1 and ADAM10 (Figure 6B and C) and thus, they enabled us to align the two sequences (Figure 6E). Based on this alignment, we completed entire alignments (Supplementary Figure 1) including 38 sequences of mammalian ADAMs and *Schizosaccharomyces pombe* Mde10 (Nakamura *et al*, 2004), presumably the founding member of the ADAM family in evolutionary terms. The ADAM10$_{D+C}$ structure lacks the eight residues (583–590 in ADAM10) that may form a flexible loop. However, VAP1 (Figure 6E) and the canonical ADAMs except for ADAM8 (Supplementary Figure 1) have extra 16 residues in this segment that, in part, forms a variable loop, flanked by the adjacent cysteinyl residues (Cys539 and Cys549 in VAP1) and protrudes from the main body of the C-domain (Figures 4A and 6B). The variable loop has highest temperature factor in the molecule and resembles to the

disintegrin-loop, thus can be an additional protein-binding interface. The six VAP1 monomer molecules represent almost the same C$_w$/C$_h$ domain orientation (data not shown), however that is distinct from that of ADAM10 (Figure 5A). Thus, the possibility whether different ADAMs have distinct C$_w$/C$_h$ domain orientation remains to be established. Janes *et al* (2005) have shown that the three glutamate residues outside of HVR are essential for ADAM10-mediated ephrin proteolysis in *trans*, however, roles of the ADAM10 HVR has not been examined. An extensive molecular surface of the elongated arm structure (12 000 Å^2 for the VAP1 D/C-domains) might reveal additional protein–protein interaction interfaces other than the HVR. Multiple charged residues in the D-domain are essential for ADAM28 binding to α4β1 (Bridges *et al*, 2003) and the RX$_6$DLPEF motif has been proposed for integrin α9β1 binding (Eto *et al*, 2002). However, the D-domain portion of the C-shaped scaffold is away from the catalytic site; thus, those additional sites might not directly serve as target recognition interfaces for catalysis.

Uniquely among cell-surface proteins, ADAMs display both proteolytic and adhesive activities. The VAP1 structure reveals that these functions are spatially allocated to the ends of the unique C-shaped scaffold and face each other. This spatial allocation of the functional sites provide us insights
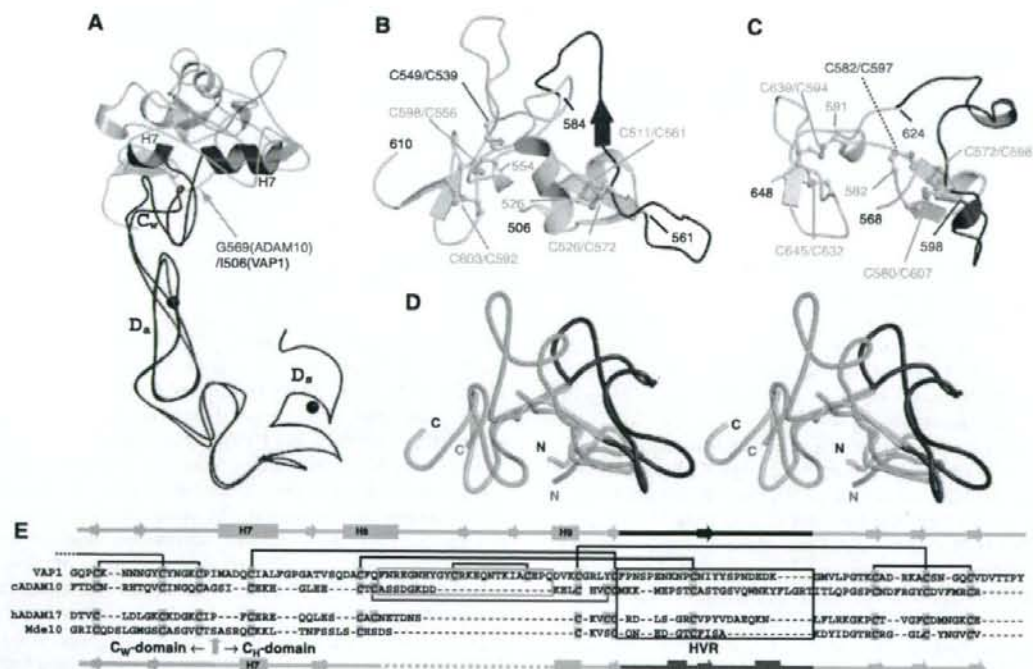

Figure 6 Comparison of the VAP1 and ADAM10 D/C domains. (**A**) Superimposition of the D$_a$-domains of ADAM10 and VAP1. The D$_s$/D$_a$/C$_w$-domains and the H7 helix of VAP1 and those of ADAM10 are shown in blue and red, respectively. The C$_h$-domains of VAP1 and ADAM10 are shown in cyan and pink, respectively. The arrow indicates the pivotal point between the C$_w$- and C$_h$-domains. Bound Ca^{2+} ions in VAP1 are shown as black spheres. (**B**) Ribbon representation of the C$_h$-domain of VAP1. The HVR is shown in blue. The common scaffold between the VAP1 and ADAM10 C$_h$-domains are shown in cyan and the segment lacking in ADAM10 is shown in light green. Disulfide bridges are indicated. (**C**) Ribbon representation of the C$_h$-domain of ADAM10. The HVR is shown in red. Disulfide brides are indicated. (**D**) Superimposition of the C$_h$-domains of VAP1 and ADAM10 *in stereo* with the colors as in (B, C). The N- and C-termini of the C$_h$-domains are indicated. (**E**) Structure-based alignments of VAP1, bovine ADAM10 (cADAM10), human ADAM17 (hADAM17) and *S. pombe* Mde10 (Mde10) C$_w$/C$_h$-domains. Secondary structures and the disulfide bridges are represented schematically. The HVR sequences and the missing segment in the ADAM10 structure are boxed in blue and green, respectively.